Journal of
Applied Physics

ARTICLE

pubs.aip.org/aip/jap

Increased thermal conductivity of β-Ga_2O_3 using Al substitution: Full spectrum phonon engineering

Cite as: J. Appl. Phys. **137**, 105701 (2025); doi: 10.1063/5.0249882
Submitted: 4 December 2024 · Accepted: 13 February 2025 ·
Published Online: 10 March 2025

Kongping Wu,[1,2,a)] Guoqing Chang,[2] Jiandong Ye,[3] and Gang Zhang[4,a)]

AFFILIATIONS

[1] School of Electronics and Information Engineering, Jinling Institute of Technology, Nanjing, Jiangsu 211169, China
[2] Division of Physics and Applied Physics, School of Physical and Mathematical Sciences, Nanyang Technological University, Singapore 637371, Singapore
[3] School of Electronic Science and Engineering, Nanjing University, Nanjing, Jiangsu 210093, China
[4] Yangtze Delta Region Academy of Beijing Institute of Technology (Jiaxing), Jiaxing 314019, China

[a)] **Authors to whom correspondence should be addressed:** kongpingwu@126.com and gangzhang2006@gmail.com

ABSTRACT

Improving the thermal conductivity of β-Ga_2O_3 is critical for optimizing its performance in high-power electronic devices, as effective thermal management significantly influences their output power and reliability. In this work, the thermal conductivities of β-Ga_2O_3 and $(Al_xGa_{1-x})_2O_3$ alloys along the $(\bar{2}\ 0\ 1)$ direction were first computed using a non-equilibrium molecular dynamics method based on the deep learning potential. Our results indicate that the calculated thermal conductivity of β-Ga_2O_3 is 16.6 W $m^{-1}K^{-1}$ along the $(\bar{2}\ 0\ 1)$ direction, which is in excellent agreement with experimental measurements. In our findings, an Al to Ga ratio of 1:1 leads to the thermal conductivity of the $(Al_xGa_{1-x})_2O_3$ alloy being more than twice that of β-Ga_2O_3, regardless of the Al substitution sites. The $(Al_{0.5}Ga_{0.5})_2O_3$ alloy exhibits enhanced thermal conductivity due to the improved transport properties of optical phonon modes, including the increased group velocities, the enhanced participation, and the induced new vibrational modes at higher frequencies. This research provides theoretical predictions regarding the optimal Al to Ga ratio to enhance the thermal conductivity of $(Al_xGa_{1-x})_2O_3$ alloys, offering crucial insights for the design and thermal management of β-Ga_2O_3 power devices.

I. INTRODUCTION

Gallium oxide (β-Ga_2O_3) is drawing widespread attention in the field of power electronics primarily due to its ultra-wide bandgap of approximately 4.8–4.9 eV,[1–3] which is significantly higher than that of GaN (3.4 eV).[4] The ultra-wide bandgap enables β-Ga_2O_3 devices to operate at an exceptionally high critical electric field (~8 MV/cm),[5] far exceeding GaN (~3.3 MV/cm).[4] This allows for the fabrication of devices that can sustain higher voltages with smaller geometries, enhancing energy efficiency and reducing size. Besides, β-Ga_2O_3 can be easily deposited using magnetron sputtering[6,7] in a low vacuum condition without worrying about oxygen, simplifying the process.

In the pursuit of high-quality β-Ga_2O_3 and its alloys for advanced power electronics applications, the choice of deposition technique plays a pivotal role. For instance, metal–organic chemical vapor deposition (MOCVD) offers precise control over the composition, doping of the films, and β-Ga_2O_3/$(Al_xGa_{1-x})_2O_3$ interfaces, albeit at the expense of a more complex setup and operational intricacies.[8–11] Similarly, molecular beam epitaxy (MBE) provides atomic layer control during the growth process, essential for creating epitaxial layers with minimal defects, yet it requires ultra-high vacuum conditions and is more suited for laboratory-scale research.[12] Hydrothermal vapor phase epitaxy (HVPE) presents another viable approach for growing high-quality β-Ga_2O_3 films,[13,14] although it involves handling hazardous gases and requires careful optimization of growth parameters.

However, one of the significant drawbacks of β-Ga_2O_3 is its poor thermal conductivity (13–22 W $m^{-1}K^{-1}$),[15,16] which is substantially lower than GaN (~230 W $m^{-1}K^{-1}$).[17] This limits heat dissipation in β-Ga_2O_3-based devices, making thermal management a critical challenge. Recently, most research has focused on measuring and theoretically calculating the thermal conductivity of pure β-Ga_2O_3,[15,16,18] and efforts to improve its thermal performance are limited.[19] This promising work was performed by Mu *et al.*,[19] which involves alloying β-Ga_2O_3 with aluminum (Al) to form $(Al_xGa_{1-x})_2O_3$ alloys, which have shown a surprising increase in thermal conductivity compared to pure β-Ga_2O_3. Although traditional first-principles approaches, which rely on three-phonon processes, are capable of incorporating anharmonic interactions at finite temperatures, they inherently exclude higher-order anharmonic effects. More importantly, $(Al_xGa_{1-x})_2O_3$ alloys could act as a buffer layer in β-Ga_2O_3-based devices,[20] significantly boosting performance and thermal management. Its adjustable bandgap and higher thermal conductivity than β-Ga_2O_3 make it ideal for managing lattice mismatches and efficiently dissipating heat, especially vital in high-power applications.

The increased thermal conductivity of $(Al_xGa_{1-x})_2O_3$ alloys may challenge conventional understanding, where the introduction of impurities into semiconductors generally decreases thermal conductivity due to enhanced anharmonic phonon scattering. The introduction of impurities into a semiconductor destroys the spatial symmetry of the system and the uniform bonding environment and also increases the disorder of the semiconductor system. All these factors in turn enhance the impurity-phonon scattering in the alloy system, leading to a decrease in the thermal conductivity of the alloy system. For instance, in GaN, the introduction of Al to form $Al_yGa_{1-y}N$ alloys results in a decrease in thermal conductivity compared to both GaN and AlN.[21,22] In this work, we found that an appropriate proportion of Al can enhance the phonon thermal conductivity of β-Ga_2O_3. And the advanced methodologies employed in our study, such as deep learning potentials and non-equilibrium molecular dynamics (NEMD) simulations, explicitly capture these higher-order effects and provide a more comprehensive understanding of the phonon transport mechanisms.

II. MACHINE LEARNING MODEL TRAINING AND COMPUTATIONAL DETAILS

The *ab initio* molecular dynamics (AIMD) was first used to calculate the atomic trajectories in the β-Ga_2O_3 and $(Al_xGa_{1-x})_2O_3$ alloys using the Vienna *Ab initio* Simulation Package code.[23] These trajectories are used to train and generate a machine learning model[24,25] that can accurately describe the interatomic potentials in β-Ga_2O_3 and $(Al_xGa_{1-x})_2O_3$ alloys. This model captures the complex interactions between atoms by learning from the high-fidelity AIMD data. The generated deep potential model, representing the interatomic potential, is finally frozen (meaning its training is complete and its parameters are fixed), and then it undergoes compression techniques to optimize its computational efficiency for large-scale molecular dynamics (MD) simulations. Freezing the model ensures that its learned parameters remain unchanged during the MD simulations, preserving the integrity of the trained interatomic potential. Compression, through methods such as parameter pruning and quantization, reduces the model's computational demands, facilitating its application in resource-intensive, large-scale MD simulations. The deep potential molecular dynamics (DeePMD) framework[25] was employed to calculate the thermal conductivities of the β-Ga_2O_3 and $(Al_xGa_{1-x})_2O_3$ alloys, which can achieve a balance between computational efficiency and accuracy, enabling the reliable prediction of thermal properties for the β-Ga_2O_3 and $(Al_xGa_{1-x})_2O_3$ alloys.

The conventional unit cell of β-Ga_2O_3 typically contains 12 O atoms and 8 Ga atoms. As illustrated in Fig. 1(a), the Ga atoms occupy two distinct sets of sites, with each set containing four atoms. One type of Ga atom is situated in an octahedral configuration (Ga_O) coordinated by six O atoms, while the other type of Ga atom is in a tetrahedral configuration (Ga_T) coordinated by four O atoms. Additionally, the $(\bar{2}\ 0\ 1)$ plane was cleaved and is shown in Fig. 1(b). In this work, we will use the NEMD method to calculate the thermal conductivity along the $(\bar{2}\ 0\ 1)$ direction. This study focuses on the $[\bar{2}\ 0\ 1]$ direction of β-Ga_2O_3 thin films, as this orientation is closely related to the practical application of β-Ga_2O_3 films grown on diamond substrates.[7] The choice of diamond substrates is due to their high thermal conductivity and the ease of achieving p-type conductivity, which provides good complementarity with β-Ga_2O_3. Nevertheless, we also acknowledge the importance of studying the [0 1 0] direction, especially for homoepitaxial growth on Ga_2O_3 single crystal substrates. The thermal conductivity in the [0 1 0] direction is significantly higher, nearly triple that of β-Ga_2O_3 films,[16] making it equally significant for the design of the $(Al_xGa_{1-x})_2O_3$/β-Ga_2O_3 structure and performance optimization of homoepitaxial devices. This enhanced thermal conductivity may offer new perspectives on device design and performance enhancement.

In the details of the computations, we employed the supercell approach to generate model thicknesses of 10.392, 20.257, 25.414, 30.122, 35.279, and 40.447 nm along the $(\bar{2}\ 0\ 1)$ direction as shown in Fig. 1(c). For each thickness, we calculated their thermal conductivities. Subsequently, we conducted a linear fitting based on the linear relationship between the reciprocal of thermal conductivity and the reciprocal of thickness. Utilizing extrapolation, we obtained the thermal conductivity of a sufficiently thick model, which approximates the thermal conductivity of experimentally bulk materials. Recent theoretical calculations have suggested that when Ga atoms in octahedral sites are substituted by Al atoms, the stable $(Al_xGa_{1-x})_2O_3$ alloys exhibit lower formation energies.[26] The crystal structure of β-Ga_2O_3 was first optimized and calculated based on DFT. The optimized structural parameters are listed in Table S1 in the supplementary materials and show excellent agreement with experimental measurements.[27] Then, we substituted Ga atoms with Al in a stepwise manner, first replacing Ga in octahedral sites and then replacing Ga in tetrahedral sites. This process generated seven different $(Al_xGa_{1-x})_2O_3$ alloys, along with a θ-Al_2O_3 structure as shown in Table S1 in the supplementary materials.

The substitution of Ga with Al offers a promising approach to tailoring the physical properties of β-Ga_2O_3, similar to the well-known $Al_yGa_{1-y}N$ system where Al is introduced into GaN to optimize performance, for example, formation of GaN/$Al_yGa_{1-y}N$ heterojunctions to enhance the electronic conductivity of the devices,[28] tuning of band structure to meet specific electrical performance requirements of the devices,[29] and improvement of material quality to enhance device reliability.[30] Besides, the structural parameters of these alloys were also calculated and are presented in Table S1 in the supplementary materials. The introduction of Al into β-Ga_2O_3 causes the lattice parameters and volume of the

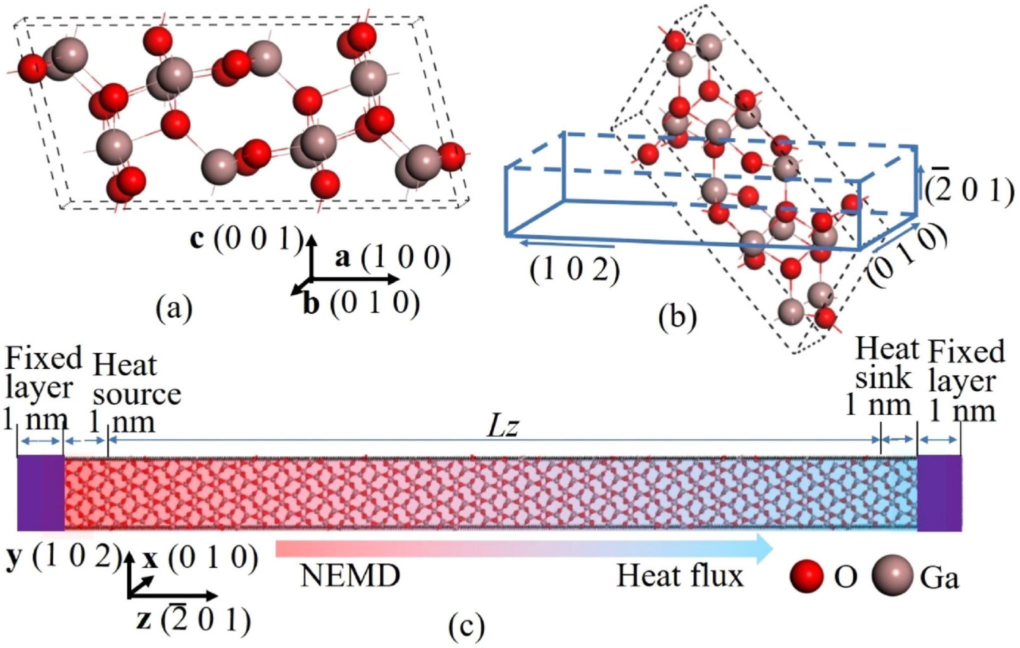

FIG. 1. (a) Conventional unit cell of β-Ga_2O_3, (b) the cleaved ($\bar{2}$ 0 1) plane of β-Ga_2O_3, and (c) the model for computing the thermal conductivity along the ($\bar{2}$ 0 1) direction based on the NEMD method.

$(Al_xGa_{1-x})_2O_3$ alloy to gradually decrease. This is expected because the atomic radius of Al is smaller than that of Ga. Besides, the phonon spectra of these alloys were computed using the Phonopy code[31] and the second-order force constants. The results are provided in the supplementary materials (as shown in Fig. S1 in the supplementary material). The phonon spectra of all $(Al_xGa_{1-x})_2O_3$ alloys exhibit no imaginary frequencies, indicating that these structures are dynamically stable.

III. RESULTS AND DISCUSSION

The AIMD simulations were used to generate MD trajectories for β-Ga_2O_3 and $(Al_xGa_{1-x})_2O_3$ alloys. In the AIMD simulation based on the canonical ensemble (NVT), the simulation duration was set to 10 ps, the temperature was maintained at 300 K, and the time step was 1 fs. These trajectories were then used to create training and validation datasets. Based on these datasets, a deep learning potential was established using the DeePMD-kit.[24,25] The control parameters for the data training process are listed in Table S2 in the supplementary materials, and the physical significance of each control parameter has been explained in detail by the DeePMD-kit developers.[32]

During data training, the loss functions for the root-mean-squared error (RMSE) of energy (E) and force (F) in both the training (Trn) and validation (Val) datasets demonstrated strong convergence after 5000 steps as illustrated in Fig. 2(a) for β-Ga_2O_3. The predicted values for energy/atom and force on atom were obtained using the deep learning potential and are shown in Figs. 2(b) and 2(c) for β-Ga_2O_3, which are in good agreement with the validation datasets from AIMD calculations. The RMSE for energy/atom and force on atom are less than 1 meV/atom and about a few dozen meV/Å, respectively. It indicates a successful training outcome for β-Ga_2O_3. Such a standard data training procedure is also used for $(Al_xGa_{1-x})_2O_3$ alloys. For $(Al_{0.5}Ga_{0.5})_2O_3$ alloys, the loss functions for the RMSE of energy and force and predicted values for energy of each atom and force on each atom are shown in Figs. 2(d)–2(f), respectively. For $(Al_{0.25}Ga_{0.75})_2O_3$ and $(Al_{0.75}Ga_{0.25})_2O_3$ alloys, the physical quantities associated with the data training process are shown in Figs. S2 and S3 in the supplementary materials.

The phonon dispersion and phonon density of states (PDOS) were first calculated by DeePMD.[15] The combination of a large-scale atomic/molecular massively parallel simulator (LAMMPS) and Phonopy codes can be used to calculate phonon dispersion and PDOS. In this process, the force constants file and the POSCAR structure file were generated by Phonolammps code.[33] With the force constants and the POSCAR, phonon dispersion and PDOS were obtained using the Phonopy code. Here, “POSCAR” stands for the file that contains the positions of atoms in a crystal structure used for computational simulations. Similarly, force constant can also be generated from the density functional perturbation theory (DFPT)[34] and then used to compute phonon dispersion and PDOS. The phonon dispersion and PDOS were computed and are shown in Fig. 3 using both methods. The phonon dispersions and PDOS of β-Ga_2O_3, $(Al_{0.25}Ga_{0.75})_2O_3$, $(Al_{0.5}Ga_{0.5})_2O_3$, and $(Al_{0.75}Ga_{0.25})_2O_3$ are shown in Figs. 3(a)–3(d), respectively.

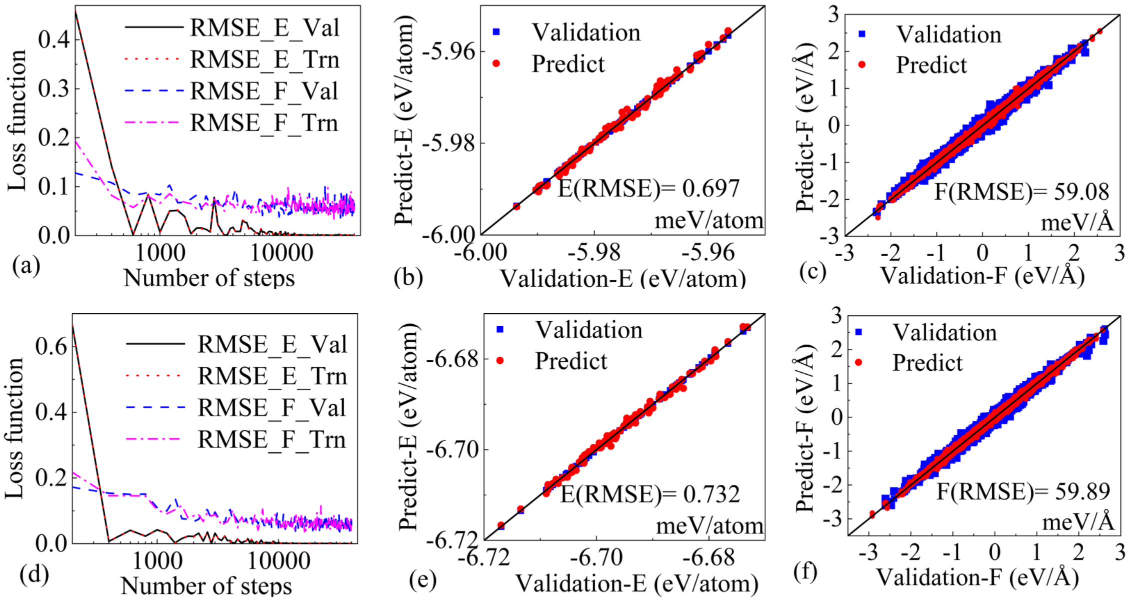

FIG. 2. (a) Loss function of the root-mean-squared error (RMSE) of energy (E) and force (F) in the training and validation datasets for β-Ga_2O_3. Comparison between prediction datasets using the deep learning potential and validation datasets from the AIMD calculation of (b) energy/atom and (c) force on atom for β-Ga_2O_3. (d) Loss function of the RMSE of energy and force in the training and validation datasets for $(Al_{0.5}Ga_{0.5})_2O_3$ alloy. Comparison between prediction datasets using the deep learning potential and validation datasets from the AIMD calculation of (e) energy/atom and (f) force on atom for $(Al_{0.5}Ga_{0.5})_2O_3$ alloy.

The computational results show that the phonon dispersion and PDOS from MD simulations using deep learning-based potentials are in good agreement with those from DFT calculations as shown in Figs. 3(a)–3(d). This demonstrates that MD simulations using deep learning potentials effectively balance the accuracy of DFT results with the efficiency of MD. Besides, the introduction of Al into β-Ga_2O_3 leads to the expansion of the phonon dispersion to higher frequencies. Moreover, the higher the content of introduced Al, the greater the extension of the phonon dispersion of the $(Al_xGa_{1-x})_2O_3$ alloys to higher frequencies as shown in Fig. 3.

The deep learning potential used to describe interatomic interactions in the β-Ga_2O_3 and $(Al_xGa_{1-x})_2O_3$ alloys has been well established. Next, the lattice thermal conductivities of the β-Ga_2O_3 and $(Al_xGa_{1-x})_2O_3$ alloys can be computed by NEMD simulations based on the generated deep learning potential. During the NEMD calculations, the boundaries at both ends of the β-Ga_2O_3 were first fixed, and then a heat source (325 K) zone and a heat sink (275 K) zone were set up at each end as shown in Fig. 1(c). This creates a temperature gradient to simulate the heat transport process, and the heat is flowing from the heat source to the heat sink along the z-direction. The time step was set to 1 fs. According to Fourier's law, the temperature gradient and heat flux can be used to calculate the thermal conductivity of β-Ga_2O_3 after the system has reached steady state. Fourier's law can be written as[35]

$$\kappa_z = \frac{Q}{\Delta T/\Delta z}, \tag{1}$$

$$Q = \frac{1}{S_{\text{int}}}\frac{dE}{dt}, \tag{2}$$

where κ_z is the thermal conductivity associated with the model size (L_z); Q is the heat flux, which can be calculated from the average of the slopes of the linear fits of the energy as a function of time for heat sources and heat sinks as shown in Fig. 4(a). And $\Delta T/\Delta z$ is the gradient of temperature at steady state in the z direction as shown in Fig. 4(b). In Eq. (2), S_{int} is the cross-sectional area of the xy-plane as shown in Fig. 1(c). The method of linear extrapolation[36] was then applied to compute the bulk thermal conductivity, which can be expressed as

$$\frac{1}{\kappa_z} = \frac{1}{\kappa_0}\left(1 + \frac{\lambda}{L_z}\right), \tag{3}$$

where κ_0 represents the bulk thermal conductivity and λ is an effective value of the mean free path for all phonons and is also a finite quantity in magnitude.

For different model lengths of the same Al composition, the linear fit curve of the reciprocal of length-dependent thermal conductivity to the reciprocal of length is shown in Fig. 4(c). For θ-Al_2O_3, the linear fit curve has been shown in Fig. S3(d) in the supplementary materials. The thermal conductivities of the $(Al_xGa_{1-x})_2O_3$ alloys obtained by linear extrapolation for different Al compositions are shown in Fig. 4(d). Besides, the reported experimental values of 13.3–14.89 W $m^{-1}K^{-1}$ for β-Ga_2O_3,[15,16,37]

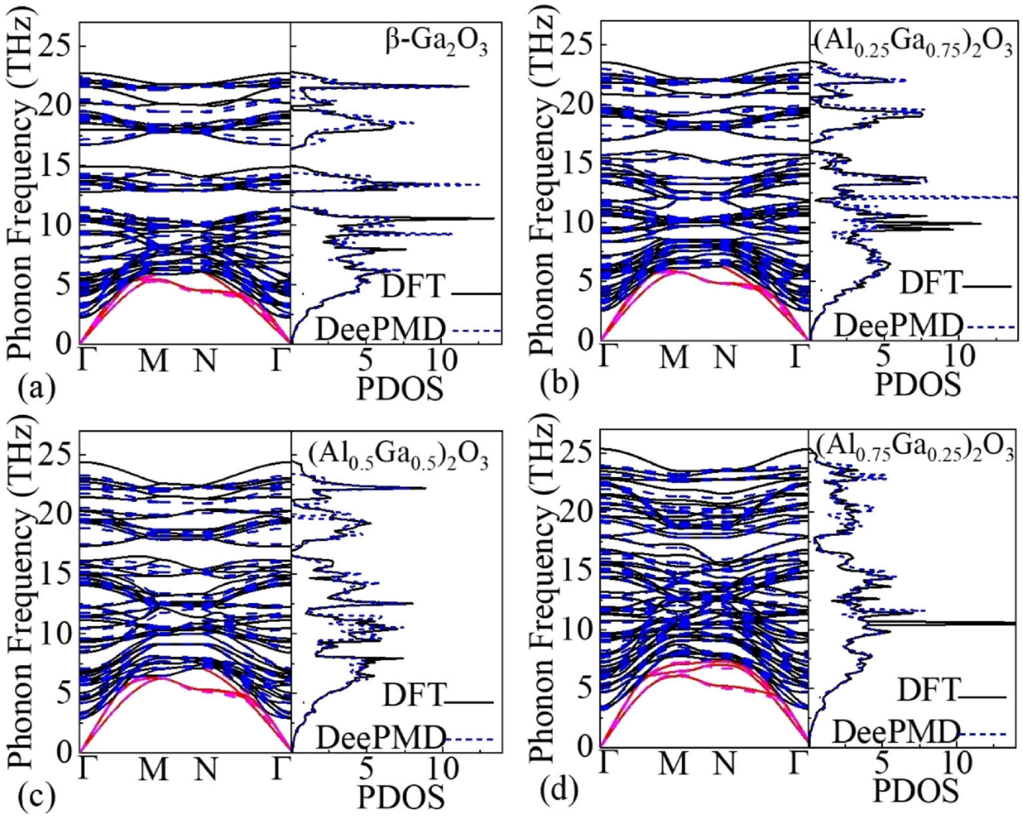

FIG. 3. Comparison of phonon dispersions and PDOS obtained by DFT and DeePMD methods for (a) β-Ga_2O_3, (b) $(Al_{0.25}Ga_{0.75})_2O_3$, (c) $(Al_{0.5}Ga_{0.5})_2O_3$, and (d) $(Al_{0.75}Ga_{0.25})_2O_3$. The red curves indicate the acoustic phonon modes.

3.13 W $m^{-1}K^{-1}$ for $(Al_{0.25}Ga_{0.75})_2O_3$,[38] and first-principle calculated value of 28 W $m^{-1}K^{-1}$ for $(Al_{0.5}Ga_{0.5})_2O_3$[19] are all shown together in Fig. 4(d). Compared to the thermal conductivities of β-Ga_2O_3, the thermal conductivity of the $(Al_{0.5}Ga_{0.5})_2O_3$ alloy increased rather than decreased. This behavior markedly differs from the U-shaped relationship observed in the thermal conductivities of the $Al_yGa_{1-y}N$ alloys as a function of the Al composition.[21]

Additionally, we substituted four Ga atoms occupying T sites with four Al atoms and successfully developed an interatomic potential that accurately describes the interactions between atoms in the $(Al_{0.5}Ga_{0.5})_2O_3$ alloy with 4 T-site Al atoms (Al_T) as shown in Figs. S4(a)–S4(c) in the supplementary materials. Based on this potential, we calculated the thermal conductivity of the $(Al_{0.5}Ga_{0.5})_2O_3$ alloy containing 4 Al_T using the linear extrapolation method. We found that the thermal conductivity of the $(Al_{0.5}Ga_{0.5})_2O_3$ alloy with 4 Al_T is comparable to that of the $(Al_{0.5}Ga_{0.5})_2O_3$ alloy with 4 Al_O atoms as shown in Fig. S4(d) in the supplementary materials, indicating that when the Al-to-Ga ratio is 1:1, the calculated thermal conductivity is more than twice that of β-Ga_2O_3, regardless of the substitution sites.

To precisely quantify the contributions of individual phonon modes and specific frequency bands to thermal transport of the β-Ga_2O_3 and $(Al_{0.5}Ga_{0.5})_2O_3$ alloys, the spectral heat current (SHC) method and phonon participation ratio (PPR) were used to calculate the spectral decomposition of thermal conductivity [$k(\omega)$] and analyze the delocalized phonon modes, respectively. The $k(\omega)$ provides detailed insight into how energy is transferred through phonons, offering a frequency-resolved picture of heat transport, where harmonic interactions and vibrational modes play significant roles. The setup was carefully designed to ensure accurate heat transport analysis. Specifically, a midplane was selected as the heat transfer interface along the direction of the ($\bar{2}$ 0 1), ensuring that the number of atoms on the left and right sides of the interface remained equal. The $k(\omega)$ as being defined by the correlation function of forces and velocities under steady-state conditions reveals how energy is transferred between atoms via their interactions. It is defined as[39,40]

$$k(\omega)=\frac{2}{S_{\text{int}}}\text{Re}\sum_{i\in\text{Left}}\sum_{j\in\text{Right}}\left[\int_{-\infty}^{+\infty}\left\langle\overrightarrow{F_{ij}(\tau)}\cdot\overrightarrow{v_i(0)}\right\rangle e^{i\omega\tau}d\tau\right], \tag{4}$$

where the harmonic force ($\overrightarrow{F_{ij}(\tau)}$) is calculated by taking the partial differential of the interaction potential U_{ij} with respect to

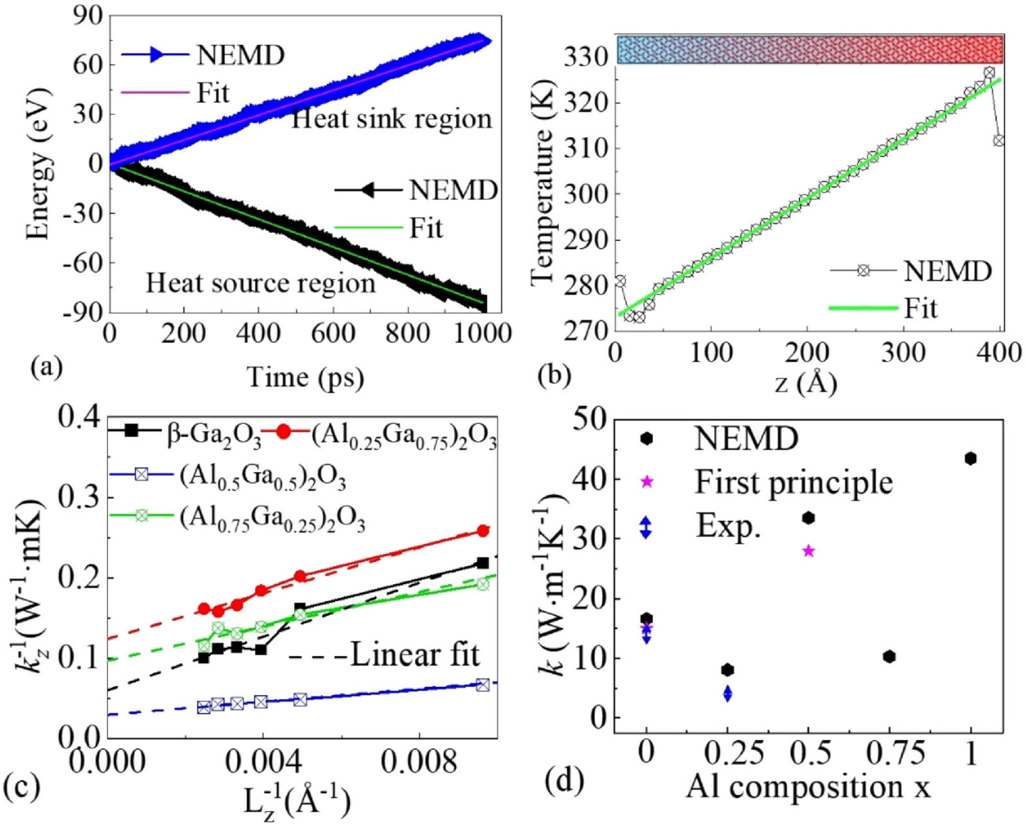

FIG. 4. (a) Relationship between the energy of the heat source and the heat sink region as a function of time, (b) temperature distribution at the model scale, (c) linear fit curve of the reciprocal of length-dependent thermal conductivity to the reciprocal of length, and (d) relationship between thermal conductivity of $(Al_xGa_{1-x})_2O_3$ alloys and Al composition.

the position expressed by position vector $\overrightarrow{r_i}$ of the ith atom at time τ, and $\overrightarrow{v_i(0)}$ is velocity of the ith atom.

In addition, the PPR quantifies the extent of spatial localization for each vibrational mode by measuring the fraction of atoms participating in that mode. It can be computed using the vibrational eigenvector components ($\varepsilon_{i\alpha,\lambda}$) of each mode ($\lambda$) in the α Cartesian direction, which describe the amplitude and phase of the ith atomic vibrations. The value of PPR was computed as follow:[41,42]

$$\mathrm{PPR}^{-1} = N\sum_i\left(\sum_\alpha \varepsilon^*_{i\alpha,\lambda}\varepsilon_{i\alpha,\lambda}\right)^2. \tag{5}$$

Based on Eq. (4), the relationship of the $k(\omega)$ with respect to frequency for β-Ga_2O_3 and $(Al_{0.5}Ga_{0.5})_2O_3$ alloys along the direction of the $(\bar{2}\ 0\ 1)$ with a length of 40.4 nm is shown in Fig. 5(a). When the Al is introduced into β-Ga_2O_3 to form the $(Al_{0.5}Ga_{0.5})_2O_3$ alloy at the Al:Ga ratio of 1:1, the thermal conductivity shows a significant increase across the entire frequency range. As depicted in Figs. 3(a) and 3(c), the phonon dispersions reveal that the incorporation of Al causes a slight shift of the phonon vibration frequencies in β-Ga_2O_3 toward higher frequencies. Notably, the acoustic phonon cut-off frequency ($f_{\text{cut-off}}$) increases from 6.03 THz in β-Ga_2O_3 to 7.47 THz in the $(Al_{0.5}Ga_{0.5})_2O_3$ alloy. Furthermore, a comparison of the $k(\omega)$ of β-Ga_2O_3 and the $k(\omega)$ of $(Al_{0.5}Ga_{0.5})_2O_3$ as shown in Fig. 5(a) indicates that the contribution from acoustic phonon vibrational modes to the increase in thermal conductivity is relatively small. Instead, the primary contribution to the enhanced thermal conductivity originates from the optical phonon vibrational modes (>7.47 THz).

The incorporation of Al in β-Ga_2O_3 alters the atomic mass distribution and bonding strength within the crystal lattice, impacting the phonon dispersion relations. Due to the lighter mass of Al and changes in interatomic forces, phonon frequencies shift to higher values, increasing lattice stiffness and enhancing phonon group velocity as shown in Fig. 5(b), particularly in the acoustic phonon regime and low-frequency optical phonon modes. According to the phonon Boltzmann transport equation,[43] the increase in group velocity plays a significant role in improving heat transport efficiency, as phonon group velocity directly influences thermal conductivity. However, the addition of Al also intensifies

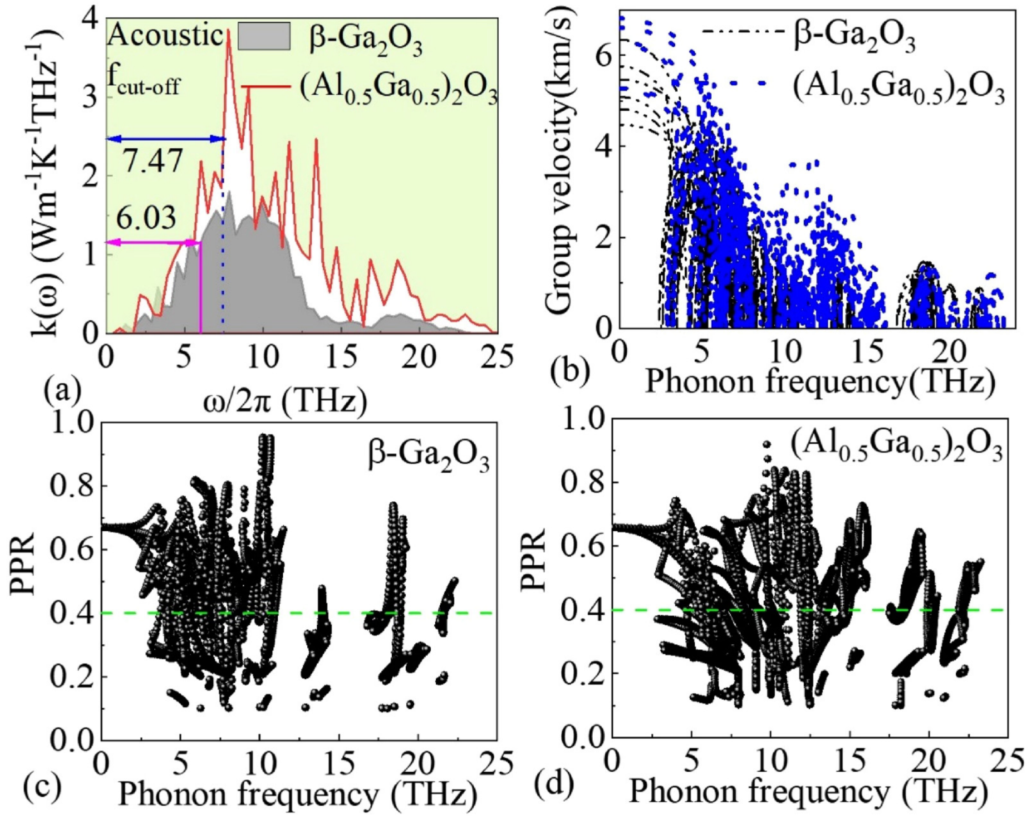

FIG. 5. (a) The spectral decomposition of thermal conductivity [$k(\omega)$] and (b) group velocity as a function of phonon frequency for β-Ga_2O_3 and $(Al_{0.5}Ga_{0.5})_2O_3$ alloy. And the phonon participation ratio vs phonon frequency for (c) β-Ga_2O_3 and (d) $(Al_{0.5}Ga_{0.5})_2O_3$, respectively.

acoustic-optical phonon scattering, reducing the lifetimes of acoustic phonons and limiting their contribution to thermal conductivity. In contrast, the altered lattice dynamics enhance the frequencies and transport properties of optical phonons, which, with longer lifetimes, become the dominant contributors to heat transport. Consequently, the overall increase in thermal conductivity in the $(Al_{0.5}Ga_{0.5})_2O_3$ alloy is primarily driven by improved optical phonon transport.

Compared to β-Ga_2O_3, $(Al_{0.5}Ga_{0.5})_2O_3$ exhibits a higher PPR, particularly in the frequency ranges associated with optical phonon modes as shown in Figs. 5(c) and 5(d). In our study, we established a critical value of 0.4 to delineate the localization status of phonons across different frequency regions.[36] Phonons within a frequency range characterized by a PPR value below this threshold are considered to be in a localized state, whereas those with a PPR value exceeding the critical value are deemed to be in a delocalized state, thereby contributing to phonon thermal conductivity. The enhanced PPR is especially pronounced in the 11–15 THz and 17.5–23 THz frequency ranges, where optical phonon modes contribute significantly. The wider frequency range and higher PPR indicate that a greater number of phonon modes, especially optical phonons, are actively involved in heat transport in $(Al_{0.5}Ga_{0.5})_2O_3$. This increased involvement aligns with the enhanced transport properties of optical phonons, which become the dominant contributors to thermal conductivity, due to the induced new vibrational modes at the higher frequencies, group velocities, and the improved PPR. Therefore, the broader and more active participation of optical phonon modes in $(Al_{0.5}Ga_{0.5})_2O_3$ is a key factor driving its higher thermal conductivity relative to β-Ga_2O_3.

IV. CONCLUSION

In conclusion, we conducted numerical training based on deep neural network models to accurately describe the interactions between atoms in β-Ga_2O_3 and $(Al_xGa_{1-x})_2O_3$ alloys. By establishing potential functions that characterize the energy and forces acting on the atoms, we were able to perform the NEMD simulations of thermal conductivities for both β-Ga_2O_3 and $(Al_xGa_{1-x})_2O_3$ alloys along the $(\bar{2}\ 0\ 1)$ direction. Our calculated thermal conductivity for β-Ga_2O_3 is 16.6 $W\,m^{-1}K^{-1}$, which aligns well with experimental values.

An exciting result in the calculated thermal conductivities is that the thermal conductivity of $(Al_{0.5}Ga_{0.5})_2O_3$ is more than double that of β-Ga_2O_3, irrespective of the Al substitution sites.

Based on the analysis of spectral thermal conductivity, group velocity, and phonon participation ratio, the enhanced thermal conductivity in $(Al_{0.5}Ga_{0.5})_2O_3$ is primarily driven by the improved transport properties of optical phonon modes. These improvements include the new phonon vibrational modes in the higher frequency, increased group velocities, and enhanced participation of optical phonon vibrational modes, which dominate heat transport compared to acoustic phonons. This work theoretically predicts that an optimal Al to Ga ratio can indeed enhance the thermal conductivity of the $(Al_xGa_{1-x})_2O_3$ alloys providing valuable insights for the design and research of β-Ga_2O_3-based power devices, particularly in the context of thermal management.

SUPPLEMENTARY MATERIAL

See the supplementary material for structural data and phonon dispersions for $(Al_xGa_{1-x})_2O_3$ alloys, deep learning training parameters and validation results for energy, and force predictions and thermal conductivity comparisons for $(Al_{0.5}Ga_{0.5})_2O_3$ alloys with different configurations.

ACKNOWLEDGMENTS

This work was financially supported by the Science Foundation of Jinling Institute of Technology (No. jit-rcyj-202001) and the scholarship from China Scholarship Council (CSC) under Grant No. 202308320197. Professor Chang is working at the Nanyang Technological University supported by the National Research Foundation, Singapore, under its Fellowship Award (No. NRF-NRFF13-2021-0010), the Agency for Science, Technology and Research (A*STAR) under its Manufacturing, Trade and Connectivity (MTC) Individual Research Grant (IRG) (Grant No. M23M6c0100), the Singapore Ministry of Education (MOE) Academic Research Fund Tier 3 Grant (No. MOE-MOET32023-0003), the Singapore Ministry of Education (MOE) AcRF Tier 2 Grant (No. MOE-T2EP50222-0014), and the Nanyang Assistant Professorship Grant (NTU-SUG).

AUTHOR DECLARATIONS

Conflict of Interest

The authors have no conflicts to disclose.

Author Contributions

Kongping Wu: Conceptualization (equal); Funding acquisition (equal); Investigation (equal); Methodology (equal); Software (equal); Writing – original draft (equal). **Guoqing Chang:** Formal analysis (equal); Funding acquisition (equal). **Jiandong Ye:** Supervision (equal); Writing – review & editing (equal). **Gang Zhang:** Supervision (equal); Writing – review & editing (equal).

DATA AVAILABILITY

The data that support the findings of this study are available from the corresponding authors upon reasonable request.

REFERENCES

[1] F. Zhou, H. H. Gong, M. Xiao, Y. W. Ma, Z. P. Wang, X. X. Yu, L. Li, L. Fu, H. H. Tan, Y. Yang, F. F. Ren, S. L. Gu, Y. D. Zheng, H. Lu, R. Zhang, Y. H. Zhang, and J. D. Ye, "An avalanche-and-surge robust ultrawide-bandgap heterojunction for power electronics," Nat. Commun. **14**, 4459 (2023).

[2] K. Sasaki, M. Higashiwaki, A. Kuramata, T. Masui, and S. Yamakoshi, "Ga_2o_3 Schottky barrier diodes fabricated by using single-crystal β-Ga_2O_3 (010) substrates," IEEE Electron Device Lett. **34**, 493 (2013).

[3] S. Dhara, N. K. Kalarickal, A. Dheenan, C. Joishi, and S. Rajan, "β-ga_2O_3 Schottky barrier diodes with 4.1 MV/cm field strength by deep plasma etching field-termination," Appl. Phys. Lett. **121**, 203501 (2022).

[4] M. Meneghini, C. D. Santi, I. Abid, M. Buffolo, M. Cioni, R. A. Khadar, L. Nela, N. Zagni, A. Chini, F. Medjdoub, G. Meneghesso, G. Verzellesi, E. Zanoni, and E. Matioli, "GaN-based power devices: Physics, reliability, and perspectives," J. Appl. Phys. **130**, 181101 (2021).

[5] M. Higashiwaki, K. Sasaki, A. Kuramata, T. Masui, and S. Yamakoshi, "Gallium oxide (Ga_2O_3) metal-semiconductor field-effect transistors on single-crystal β-Ga_2O_3 (010) substrates," Appl. Phys. Lett. **100**, 013504 (2012).

[6] M. Cui, Y. J. Zhang, S. H. Gu, C. D. Zhang, F. F. Ren, D. M. Tang, Y. Yang, S. L. Gu, R. Zhang, and J. D. Ye, "Unraveling evolution of microstructural domains in the heteroepitaxy of β-Ga_2O_3 on sapphire," Appl. Phys. Lett. **124**, 122103 (2024).

[7] T. Kusaba, P. Sittimart, Y. Katamune, T. Kageura, H. Naragino, S. Ohmagari, S. M. Valappil, S. Nagano, A. Zkria, and T. Yoshitake, "Heteroepitaxial growth of β-Ga_2O_3 thin films on single crystalline diamond (111) substrates by radio frequency magnetron sputtering," Appl. Phys. Express **16**, 105503 (2023).

[8] M. Bosi, P. Mazzolini, L. Seravalli, and R. Fornari, "Ga_2o_3 polymorphs: Tailoring the epitaxial growth conditions," J. Mater. Chem. C **8**, 10975 (2020).

[9] F. Egyenes-Pörsök, F. Gucmann, K. Hušeková, E. Dobročka, M. Sobota, M. Mikolášek, K. Fröhlich, and M. Ťapajna, "Growth of α- and β-Ga_2O_3 epitaxial layers on sapphire substrates using liquid-injection MOCVD," Semicond. Sci. Technol. **35**, 115002 (2020).

[10] D. Gogova, G. Wagner, M. Baldini, M. Schmidbauer, K. Irmscher, R. Schewski, Z. Galazka, M. Albrecht, and R. Fornari, "Structural properties of Si-doped β-Ga_2O_3 layers grown by MOVPE," J. Cryst. Growth **401**, 665 (2014).

[11] F. Hrubišák, K. Hušeková, X. Zheng, A. Rosová, E. Dobročka, M. Ťapajna, M. Mičušík, P. Nádaždy, F. Egyenes, J. Keshtkar, E. Kováčová, J. W. Pomeroy, M. Kuball, and F. Gucmann, "Heteroepitaxial growth of Ga_2O_3 on 4H-SiC by liquid-injection MOCVD for improved thermal management of Ga_2O_3 power devices," J. Vac. Sci. Technol. A **41**, 042708 (2023).

[12] N. Nepal, D. S. Katzer, B. P. Downey, V. D. Wheeler, L. O. Nyakiti, D. F. Storm, M. T. Hardy, J. A. Freitas, E. N. Jin, D. Vaca, L. Yates, S. Graham, S. Kumar, and D. J. Meyer, "Heteroepitaxial growth of β-Ga_2O_3 films on SiC via molecular beam epitaxy," J. Vac. Sci. Technol. A **38**, 063406 (2020).

[13] Y. W. Li, X. Q. Xiu, W. L. Xu, L. Y. Zhang, H. Zhao, Z. L. Xie, T. Tao, P. Chen, B. Liu, R. Zhang, and Y. D. Zheng, "Pure-phase κ-Ga_2O_3 layers grown on c-plane sapphire by halide vapor phase epitaxy," Superlattices Microstruct. **152**, 106845 (2021).

[14] B. R. Tak, S. Kumar, A. K. Kapoor, D. Wang, X. Li, H. Sun, and R. Singh, "Recent advances in the growth of gallium oxide thin films employing various growth techniques—A review," J. Phys. D: Appl. Phys. **54**, 453002 (2021).

[15] X. L. Xiao, Y. L. Mao, B. W. Meng, G. Ma, K. Hušeková, F. Egyenes, A. Rosová, E. Dobročka, P. Eliáš, M. Ťapajna, F. Gucmann, and C. Yuan, "Phase-dependent phonon heat transport in nanoscale gallium oxide thin films," Small **20**, 2309961 (2024).

[16] Z. Guo, A. Verma, X. F. Wu, F. Y. Sun, A. Hickman, T. Masui, A. Kuramata, M. Higashiwaki, D. Jena, and T. F. Luo, "Anisotropic thermal conductivity in single crystal β-gallium oxide," Appl. Phys. Lett. **106**, 111909 (2015).

[17] C. Mion, J. F. Muth, E. A. Preble, and D. Hanser, "Accurate dependence of gallium nitride thermal conductivity on dislocation density," Appl. Phys. Lett. **89**, 092123 (2006).

[18] Z. P. Sun, Z. J. Qi, K. Liang, X. Sun, Z. F. Zhang, L. J. Li, Q. J. Wang, G. Q. Zhang, G. Wu, and W. Shen, "A neuroevolution potential for predicting the thermal conductivity of α, β, and ϵ-Ga_2O_3," Appl. Phys. Lett. **123**, 192202 (2023).

[19] S. Mu, H. Peelaers, and C. G. Van de Walle, "*Ab initio* study of enhanced thermal conductivity in ordered $AlGaO_3$ alloys," Appl. Phys. Lett. **115**, 242103 (2019).

[20] Y. L. Cheng, C. F. Zhang, Y. Xu, Z. Li, D. Z. Chen, W. D. Zhu, Q. Feng, S. R. Xu, J. C. Zhang, and Y. Hao, "Heteroepitaxial growth of β-Ga_2O_3 thin films on c-plane sapphire substrates with β-$(Al_xGa_{1-x})_2O_3$ intermediate buffer layer by mist-CVD method," Mater. Today Commun. **29**, 102766 (2021).

[21] D. Q. Tran, R. Delgado-Carrascon, J. F. Muth, T. Paskova, M. Nawaz, V. Darakchieva, and P. P. Paskov, "Phonon-boundary scattering and thermal transport in $Al_xGa_{1-x}N$: Effect of layer thickness," Appl. Phys. Lett. **117**, 252102 (2020).

[22] K. P. Wu, G. Q. Chang, J. D. Ye, and G. Zhang, "Significantly enhanced interfacial thermal conductance across GaN/diamond interfaces utilizing $Al_xGa_{1-x}N$ as a phonon bridge," ACS Appl. Mater. Interfaces **16**, 58880 (2024).

[23] J. L. Wormald and A. I. Hawari, "Generation of phonon density of states and thermal scattering law using *ab initio* molecular dynamics," Prog. Nucl. Energy **101**, 461 (2017).

[24] R. Y. Li, Z. Y. Liu, A. Rohskopf, K. Gordiz, A. Henry, E. Lee, and T. F. Luo, "A deep neural network interatomic potential for studying thermal conductivity," Appl. Phys. Lett. **117**, 152102 (2020).

[25] H. Wang, L. F. Zhang, J. Q. Han, and W. N. E, "DeePMD-kit: A deep learning package for many-body potential energy representation and molecular dynamics," Comput. Phys. Commun. **228**, 178 (2018).

[26] H. Peelaers, J. B. Varley, J. S. Speck, and C. G. Van de Walle, "Structural and electronic properties of Ga_2O_3-Al_2O_3 alloys," Appl. Phys. Lett. **112**, 242101 (2018).

[27] J. Åhman, G. Svensson, and J. Albertsson, "A reinvestigation of β-gallium oxide," Acta Cryst. **C52**, 1336 (1996).

[28] J. H. Li, W. H. Yang, S. Q. Li, H. Y. Chen, D. Y. Liu, and J. Y. Kang, "Enhancement of p-type conductivity by modifying the internal electric field in Mg- and Si-δ-codoped $Al_xGa_{1-x}N/Al_yGa_{1-y}N$ superlattices," Appl. Phys. Lett. **95**, 151113 (2009).

[29] D. J. As, T. Frey, M. Bartels, K. Lischka, R. Goldhahn, S. Shokhovets, A. Tabata, J. R. L. Fernandez, and J. R. Leite, "MBE growth of cubic $Al_yGa_{1-y}N$/GaN heterostructures structural, vibrational and optical properties," J. Cryst. Growth **230**, 421 (2001).

[30] M. Gladysiewicz, D. Hommel, and R. Kudrawiec, "Material gain engineering in staggered polar AlGaN/AlN quantum wells dedicated for deep UV lasers," IEEE J. Sel. Top. Quantum Electron. **25**, 1 (2019).

[31] A. Togo, "First-principles phonon calculations with phonopy and Phono3py," J. Phys. Soc. Jpn. **92**, 012001 (2023).

[32] J. Z. Zeng, D. Zhang, D. H. Lu, P. Mo, Z. Li, Y. Chen, M. Rynik, L. Huang, Z. Li, S. Shi, Y. Wang, H. Ye, P. Tuo, J. Yang, Y. Ding, Y. Li, D. Tisi, Q. Zeng, H. Bao, Y. Xia, J. Huang, K. Muraoka, Y. Wang, J. Chang, F. Yuan, S. L. Bore, C. Cai, Y. Lin, B. Wang, J. Xu, J.-X. Zhu, C. Luo, Y. Zhang, R. E. A. Goodall, W. Liang, A. K. Singh, S. Yao, J. Zhang, R. Wentzcovitch, J. Han, J. Liu, W. Jia, D. M. York, W. E, R. Car, L. Zhang, and H. Wang, "DeePMD-kit v2: A software package for deep potential models," J. Chem. Phys. **159**, 054801 (2023).

[33] T. Q. Wan, C. X. Luo, Y. Sun, and R. M. Wentzcovitch, "Thermoelastic properties of bridgmanite using deep-potential molecular dynamics," Phys. Rev. B **109**, 094101 (2024).

[34] A. Togo, F. Oba, and I. Tanaka, "First-principles calculations of the ferroelastic transition between rutile-type and $CaCl_2$-type SiO_2 at high pressures," Phys. Rev. B **78**, 134106 (2008).

[35] A. Dhar, "Heat transport in low-dimensional systems," Adv. Phys. **57**, 457 (2008).

[36] K. P. Wu, L. Zhang, F. Z. Li, L. W. Sang, M. Y. Liao, K. Tang, J. D. Ye, and S. L. Gu, "Enhancement of interfacial thermal conductance by introducing carbon vacancy at the Cu/diamond interface," Carbon **223**, 119021 (2024).

[37] M. D. Santia, N. Tandon, and J. D. Albrecht, "Lattice thermal conductivity in β-Ga_2O_3 from first principles," Appl. Phys. Lett. **107**, 41907 (2015).

[38] Y. W. Song, P. Ranga, Y. Y. Zhang, Z. Feng, H.-L. Huang, M. D. Santia, S. C. Badescu, C. U. Gonzalez-Valle, C. Perez, K. Ferri, R. M. Lavelle, D. W. Snyder, B. A. Klein, J. Deitz, A. G. Baca, J.-P. Maria, B. Ramos-Alvarado, J. Hwang, H. Zhao, X. Wang, S. Krishnamoorthy, B. M. Foley, and S. Choi, "Thermal conductivity of β-phase Ga_2O_3 and $(Al_xGa_{1-x})_2O_3$ heteroepitaxial thin films," ACS Appl. Mater. Interfaces **13**, 38477 (2021).

[39] K. Sääskilahti, J. Oksanen, J. Tulkki, and S. Volz, "Role of anharmonic phonon scattering in the spectrally decomposed thermal conductance at planar interfaces," Phys. Rev. B **90**, 134312 (2014).

[40] K. Xu, S. C. Deng, T. Liang, X. Z. Cao, M. Han, X. L. Zeng, Z. S. Zhang, N. Yang J, and Y. Wu, "Efficient mechanical modulation of the phonon thermal conductivity of Mo_6S_6 nanowires," Nanoscale **14**, 3078 (2022).

[41] A. Bodapati, P. K. Schelling, S. R. Phillpot, and P. Keblinski, "Vibrations and thermal transport in nanocrystalline silicon," Phys. Rev. B **74**, 245207 (2006).

[42] C. P. Lin, X. B. Chen, and X. L. Zou, "Phonon-grain-boundary-interaction-mediated thermal transport in Two-dimensional polycrystalline MoS_2," ACS Appl. Mater. Interfaces **11**, 25547 (2019).

[43] A. J. H. McGaughey, A. Jain, H. Y. Kim, and B. Fu, "Phonon properties and thermal conductivity from first principles, lattice dynamics, and the Boltzmann transport equation," J. Appl. Phys. **125**, 011101 (2019).